



Large-eddy simulation of turbulent flow over an array of wall-mounted cubes submerged in an emulated atmospheric boundary-layer

M. Saeedi

Aerospace Engineering Department, Amirkabir University of Technology, Tehran, Iran

ABSTRACT: Turbulent flow over an array of wall-mounted cubic obstacles has been numerically investigated using large-eddy simulation. The simulations have been performed using high-performance computations with local cluster systems. The array of cubes is fully submerged in a simulated deep rough-wall atmospheric boundary-layer with high turbulence intensity characteristics of environmental turbulent flows. Four different approaches have been tested to reproduce the approaching highly turbulent inflow condition. Significant influence of the inlet boundary condition on the predictive streamwise root mean squared velocity (and second-order turbulence statistics if generalized) have been observed. A proposed method based on inserting a solid grid at the inlet of the domain with superimposed correlated random fluctuations has been selected as the inlet boundary condition to conduct the simulations. Three different subgrid-scale (SGS) models have been also used to compare their predictive performance in turbulence statistics and temporal energy spectra. It was observed that the choice SGS model does not have considerable effect on the second-order turbulence statistics, however, it was influential on the predicted energy level in the energy spectra. It was also observed that the flow reaches a self-similar states after the second row of obstacles which was different from the reported value in some of the previous studies.

Review History:

Received: 2019-01-09
Revised: 2019-05-05
Accepted: 2019-08-04
Available Online: 2019-12-01

Keywords:

large-eddy simulation
inlet boundary condition
atmospheric boundary-layer
turbulence intensity
subgrid-scale models

1. Introduction

The massively developing urban areas with different buildings in proximity of each other, makes it an important topic to study wind engineering to understand the mechanism of flow-structure interactions. To this purpose, extensive experimental and numerical studies have been conducted to investigate turbulent flows around wall-mounted obstacles and buildings.

1.1. Experimental studies

Castro and Robins [1] studied the flow physics and wake characteristics of flow around a wall-mounted cube based on wind-tunnel experiments. They examined two different types of approaching flows, namely: irrotational uniform flow and turbulent shear flow, and revealed that the wake size is reduced when the approaching flow is a turbulent shear flow rather than a uniform flow. Okajima [2] investigated the effects of aspect ratio of wall-mounted rectangular obstacles on the vortex shedding Strouhal number and the flow pattern. It was shown that for a certain range of Reynolds number and for width-to-height ratio of 2 and 3, the flow pattern would abruptly change with a sudden discontinuity of Strouhal number. The critical Reynolds number was assumed to be dependent on both aspect ratio and freestream turbulence while the freestream turbulence

*Corresponding author's email: Mohammad.Saeedi@aut.ac.ir

was kept constant at 0.5%. Hussein and Martinuzzi [3] studied the three dimensional flow structures around a wall-mounted cube in a water-channel experiment. They defined four critical regions of the flow, i.e.: 1) upstream region in which the obstacle effect was insignificant, 2) evolving shear layer on the top edge of the cube, 3) horseshoe vortex legs in the cube's wake region, and 4) far wake region in which the flow adjusts itself to a far wake. Brown et al. [4] performed high resolution measurements of first- and second-order turbulence statistics along the centerline plane of a two dimensional (2-D) array of wide buildings and a three dimensional (3-D) array of cubical buildings immersed in a simulated atmospheric boundary-layer. The goal of their experiment was to provide a high resolution experimental data for assessment of CFD codes. Sumner et al. [5, 6, 7] conducted wind-tunnel experiments to study the wake structures of a circular wall-mounted cylinder with different aspect ratios partially immersed in a boundary layer. They showed that the wake pattern and the power spectra would have similar behavior for aspect ratios between 5-9 while they would show considerably different behavior for aspect ratio 3. Martinuzzi and Havel [8] investigated the vortex shedding from two wall-mounted cubes in a tandem configuration. They conducted their experiment in a wind tunnel and did their measurements using Laser Doppler Velocimetry (LDV). They showed that for a specific range



of separation length between the cubes, shedding frequency scaled inversely with that length in a way that the Strouhal number would remain constant.

Sumner et al. [9] investigated the Strouhal number change for two circular wall-mounted cylinders in different positions relative to the freestream flow. They showed that when two cylinders were close to each other, the flow pattern was similar to a single bluff body while when the cylinders were moderately separated, two different Strouhal numbers were observable depending on the incidence angle of the connecting line between two cylinders. However, when two cylinders were separated by a distance more than 2.5 cylinder diameter, the Strouhal numbers were close to that of a single cylinder. Lim et al. [10] studied the turbulent flow over a cubic bluff body based on a wind tunnel experiment. They showed that the generally accepted assumption of Reynolds-number independency for bluff bodies submerged in thick boundary layers was not valid under all circumstances. Wang et al. [11] experimentally studied the turbulent momentum and heat transport in the wake region of a wall-mounted cylinder in both water- and wind-tunnels. The cylinder aspect ratio was between 3-7 and the it was heated in such a way that the heat could be considered as a passive scalar. It was observed in their study that the cylinder aspect ratio would affect the Reynolds stress and heat flux. They stated that the down-wash flow acted to suppress the spanwise vortices and separated two rows of spanwise vortices away from the wake center-line. Wang and Zhou [12] conducted wind-tunnel experiments using hot-wire anemometry and particle-image velocimetry (PIV) to analyze the wake region of a square cylinder of different aspect ratios. They characterized the near wake region by the interaction of the tip, base and spanwise vortices. Sattari et al. [13, 14] conducted a wind-tunnel experiment to investigate the shedding process in the near wake of a rectangular wall-mounted cylinder with aspect ratio 4. They used PIV and hot-wire anemometry for velocity measurements and pressure transducers for pressure measurements and observed two dominant regimes of vortex shedding, i.e.: A) an alternate Kármán-like shedding process and B) a pair of co-existing vortices which were present throughout a shedding cycle.

1.2. Numerical studies

Traditionally, numerical studies heavily relied on the Reynolds-averaged Navier-Stokes (RANS) approach, which however, cannot provide detailed temporal and spatial information. Lien et al. [15] compared the predictive performance of four different k - ϵ models in simulating disturbed flow over and through a two-dimensional array of rectangular buildings immersed in a deep rough-wall turbulent boundary-layer. They showed that the non-linear k - ϵ model had the best performance among the tested RANS models. Lien and Yee [16] studied turbulent flow over an array of three-dimensional buildings using two versions of k - ϵ model.

They could obtain good agreement with the experimental

results for the mean velocities but underpredicted the turbulent kinetic energy (TKE) above the buildings. Santiago et al. [17] conducted a RANS simulation with standard k - ϵ model to study the turbulent flow over a regular array of cubes submerged in an atmospheric boundary-layer. They showed that the center of the canyon vortex was located at 3/4 of the cube height and the down-wash flow

was more dominant than the up-wash flow inside the canyon region.

With the fast development of computational technology, high-resolution 3-D numerical simulations have become more and more accessible. Shah et al. [18] studied the flow over a wall-mounted cube at high Reynolds numbers using the large-eddy simulation (LES) approach and compared his simulation results against the experimental measurement data of Martinuzzi and Tropea [19]. One of their major objectives was to demonstrate the capability of LES to solve complex 3-D flows. Schmidt and Thiele [20] studied the capability of different turbulence modeling approaches in capturing the complex 3-D flow features over wall mounted cubes, and demonstrated the effectiveness of detached eddy simulation (DES) in resolving the dominant flow patterns. Hanna et al. [21] performed LES over different arrays of wall-mounted cubic obstacles immersed in a fully developed boundary-layer. They compared regular and staggered arrays of obstacles and showed that the so-called channeling effect was enhanced in the regular array configuration compared to that in the staggered configuration. They also showed that the flow reached a near-equilibrium state in both configurations after the third or fourth row. Ni'ceno et al. [22] conducted an LES over a matrix of wall-mounted internally heated cubes. They investigated the vortical structure and convective heat transfer around the cubes and showed that the total heat transfer from the cubes to the fluid was directly related to the coherent vortical structure close to the cubes.

Cheng et al. [23] compared the effectiveness of LES and RANS approaches in simulating the turbulent flow over a matrix of cubes at a relatively low Reynolds number. They showed the better performance of LES especially in prediction of Reynolds stress and spanwise mean velocity. Afgan et al. [24] conducted LES of turbulent flow over two wall-mounted circular cylinders with aspect ratios 6 and 10 and showed that the effect of the free-end down-wash flow on the wake region is stronger for the lower aspect ratio. Shi et al. [25] performed LES of wind field over a group of buildings in a staggered arrangement. They showed that the predicted turbulent fluctuation would be considerably lower than the experimentally measured values if no perturbation was used at the inlet of the computational domain and applied time-correlated random fluctuations as a remedy to this problem. Lee et al. [26] conducted a DNS to investigate the 3-D turbulent boundary-layer roughened with a staggered array of cubes and compared that with a boundary-layer flow over a 2-D rod-roughened wall. It was shown in their study that the friction velocity over a wall with 3-D roughness elements was smaller than that with 2-D roughness.

Although there have been some studies based on direct

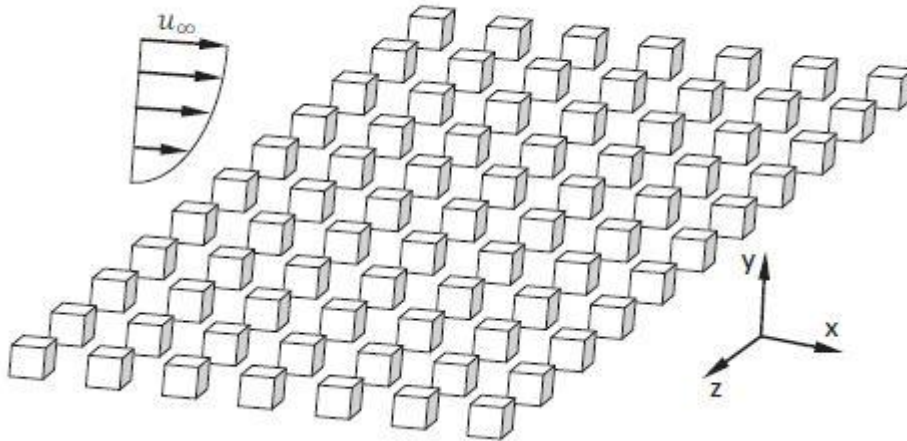


Fig. 1: Schematic of the array of 7×11 wall-mounted cubes.

numerical simulation (DNS) of flow around bluff bodies, conducting a DNS over an array of obstacles at a high Reynolds number of practical interest can be prohibitively expensive due to the demand for high resolution mesh near a large number of solid surfaces. Furthermore, detailed flow information at the finest Kolmogorov scales obtained from DNS is not always necessary in engineering practice. In view of this, LES can be an optimum tool for simulating turbulent flows and investigating detailed flow structures over an idealized urban area.

As a completion of the previously presented conference paper [27], in the current research article, we perform a high-resolution LES over an array of 3-D wall-mounted obstacles and conduct a comparative study of different inlet boundary conditions. Three SGS stress models have been tested and the obtained numerical results are validated against the available experimental data to compare the predictive performances of the SGS stress models.

2. Simulation set-up and numerical schemes

The simulation is to reproduce the experiment of Brown et al. [4] conducted at the U.S. Environmental Protection Agency's (EPA) meteorological wind tunnel. In this experiment, a regular array of 77 (7 rows by 11 columns) cubes with side-length of $h = 15$ cm are immersed in an emulated neutrally stratified atmospheric boundary layer. The cubes are strictly aligned with a uniform spacing of h in the streamwise and spanwise directions. The Reynolds number based on the cube side and mean freestream velocity is 30,000. Mean and turbulent velocities along the center line plane (plane of symmetry) are measured using a high resolution pulsed-wire anemometer.

Fig. 1 shows the schematic view of the array of cubes and the coordinate system. Given the fact that the flow domain is symmetric in the spanwise direction, only the central column (7×1 cubes) has been considered with a periodic boundary condition applied to the spanwise direction following the approach of Lien and Yee [16]. In total, $1000 \times 112 \times 128$ grid-points are used to discretize the domain in the streamwise, vertical and spanwise directions

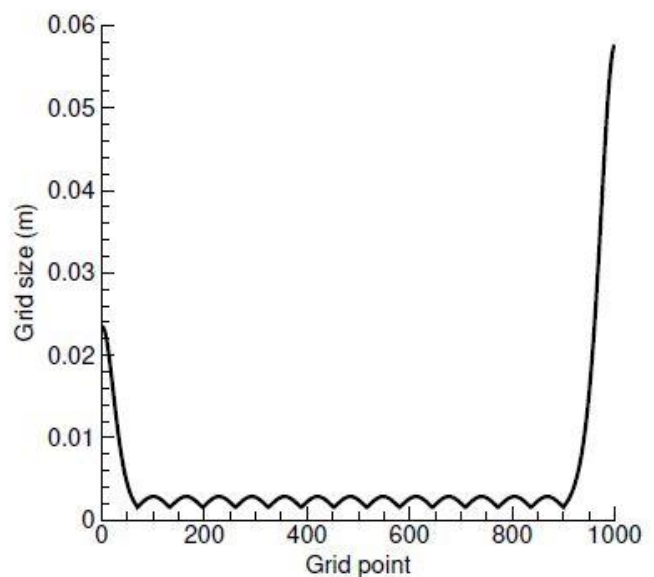


Fig. 2: Grid-size distribution in streamwise direction.

respectively. Fig. 2 shows the non-uniform grid distribution in the streamwise direction. As is evident in the figure, the grid size has its minimum value in the vicinity of solid walls. Since no wall model is applied to the governing equations and the flow dynamics is intended to be directly resolved in wall regions, it is essential to keep the non-dimensional distance of the first grid point off solid surfaces at the order of one. Also, the grid size is smoothly stretched to avoid any sudden change (which may lead to numerical error and instability) and to maintain a global second-order truncation error. In this particular case, the growth rate has been kept less than 10% to guarantee a smooth and gradual growth for the grid-size. According to Madabhushi and Vanka [28], a slow growth rate of the grid size is required in order to maintain a global second-order truncation error in non-uniform grid systems. The same criterion has been applied to the grid distribution in wall-normal and spanwise directions. It must be noted that the simulation is based on implicit LES approach in which the

the threshold of modeled and computed scales directly depends on filter size and consequently the grid resolution [29]. As such, implicit LES is not a grid-independent simulation and the finer the computational grid, the more the directly computed scales of the flow.

The numerical simulations were performed using an in-house code developed using the FORTRAN 90/95 programming language, and fully-parallelized using the message passing interface (MPI) library. The code is based on a fully implicit fractional step method and fully conservative finite difference discretization scheme on a staggered grid arrangement [30]. Numerical simulations were conducted on a local 252-core computer cluster. In total, 45,000 CPU-hours have been spent to perform each simulation.

2.1. Governing equations and subgrid-scale models

Tensorial form of the filtered continuity and momentum equations in a Cartesian coordinate system take the following form for an incompressible fluid flow:

$$\frac{\partial \bar{u}_i}{\partial x_i} = 0, \quad (1)$$

$$\frac{\partial \bar{u}_i}{\partial t} + \bar{u}_j \frac{\partial \bar{u}_i}{\partial x_j} = \frac{-1}{\rho} \frac{\partial \bar{p}}{\partial x_i} + \nu \frac{\partial^2 \bar{u}_i}{\partial x_j \partial x_j} - \frac{\partial \tau_{ij}}{\partial x_j}, \quad (2)$$

in which \bar{u} and \bar{p} represent the filtered velocity and pressure fields respectively, x_i is the coordinates, and ρ and ν are the density and kinematic viscosity, respectively. τ_{ij} is the subgrid-scale (SGS) stress tensor which is essentially modeled in LES. The SGS models used in this research will be introduced at the end of this subsection. A fully implicit four-level fractional step method coupled with a second-order Crank-Nicolson scheme was used to advance the velocity field over a single time step. In the following, the semi-discretized form of the fractional step method is presented. For simplicity, the bar-sign has been removed and the ν_{eq} accounts for both fluid's and turbulent kinematic viscosity.

$$\frac{u_i^* - u_i^n}{\Delta t} + \frac{1}{4} \frac{\partial (u_j^n + u_j^*) (u_i^n + u_i^*)}{\partial x_j} = \frac{-1}{\rho} \frac{\partial p^n}{\partial x_i} + \frac{\nu_{eq}}{2} \frac{\partial^2 (u_i^n + u_i^*)}{\partial x_j \partial x_j}, \quad (3)$$

$$\frac{(u_i^{**} - u_i^*)}{\Delta t} = \frac{1}{2\rho} \frac{\partial p^n}{\partial x_i}, \quad (4)$$

$$\frac{\partial^2 p^{n+1}}{\partial x_i \partial x_i} = \frac{2\rho}{\Delta t} \frac{\partial u_i^{**}}{\partial x_i}, \quad (5)$$

$$\frac{(u_i^{n+1} - u_i^{**})}{\Delta t} = \frac{-1}{2\rho} \frac{\partial p^{n+1}}{\partial x_i}. \quad (6)$$

Here, u_i^n and u_i^{n+1} are the velocity vectors at the previous and current time steps respectively, u_i^* and u_i^{**} are two intermediate velocity components, and p^n and p^{n+1} are also the old and new pressures, respectively. In the first step, an intermediate velocity based on the pressure of previous time step is calculated using an alternative directional implicit (ADI) solver, and then in the second step, it is further modified to the second intermediate velocity by removing half of the old pressure. In the third step, the Poisson equation is solved using a four-level V-cycle multi-grid solver to obtain the new pressure field. Finally, half of the new pressure is used to update the velocity field.

Three SGS models have been used for conducting the simulation. The modeling equations for the SGS stresses are briefly described as follows. The first model is the conventional dynamic Smagorinsky model (DSM), which expresses the SGS stress tensor as

$$\tau_{ij}^* \stackrel{\text{def}}{=} \tau_{ij} - \frac{\tau_{kk}}{3} \delta_{ij} = -2C_s \bar{\Delta}^2 |\bar{S}_{ij}| \bar{S}_{ij}, \quad (7)$$

where $\bar{S}_{ij} \stackrel{\text{def}}{=} (\partial \bar{u}_i / \partial x_j + \partial \bar{u}_j / \partial x_i) / 2$ is the resolved strain rate tensor, $|\bar{S}_{ij}|$ is the norm of \bar{S}_{ij} , δ_{ij} is the Kronecker delta, and an asterisk superscript denotes the trace free form of a tensor. The model coefficient C_s is dynamically calculated as

$$C_s = - \frac{M_{ij} \mathcal{L}_{ij}}{M_{mn} M_{mn}}, \quad (8)$$

where \mathcal{L}_{ij} is the resolved Leonard type stress defined as $\mathcal{L}_{ij} \stackrel{\text{def}}{=} \bar{u}_i \bar{u}_j - \bar{u}_i \bar{u}_j$, and $M_{ij} \stackrel{\text{def}}{=} \alpha_{ij} - \beta_{ij}$ is a differential tensor. Here, $\alpha_{ij} \stackrel{\text{def}}{=} 2\bar{\Delta}^{-2} |\bar{S}_{ij}|$ and $\beta_{ij} \stackrel{\text{def}}{=} 2\bar{\Delta}^2 |\bar{S}_{ij}|$ are the test-grid and grid level base stress tensors, respectively.

The second model is the dynamic two parameter mixed model (DTPMM) of Morinishi and Vasilyev [33] which calculates the SGS stress as:

$$\tau_{ij}^* = -2C_s \bar{\Delta}^2 |\bar{S}_{ij}| \bar{S}_{ij} + C_L L_{ij}^*, \quad (9)$$

in which L_{ij} is the resolved Leonard type stress defined as $L_{ij} \stackrel{\text{def}}{=} \bar{u}_i \bar{u}_j - \bar{u}_i \bar{u}_j$. The two coefficients can be determined using the least squares approach,

$$\begin{bmatrix} H_{ij}^{Z*} H_{ij}^{Z*} & -H_{ij}^{Z*} M_{ij} \\ -H_{ij}^{Z*} M_{ij} & M_{ij} M_{ij} \end{bmatrix} \cdot \begin{bmatrix} C_L \\ C_s \end{bmatrix} = \begin{bmatrix} L_{ij}^* H_{ij}^{Z*} \\ L_{ij}^* M_{ij} \end{bmatrix}, \quad (10)$$

where $H_{ij}^Z = \bar{u}_i \bar{u}_i - \bar{u}_i \bar{u}_i$.

The third model is the dynamic non-linear model (DNM) proposed by Wang and Bergstrom [34]

$$\tau_{ij}^* = -C_S \beta_{ij} - C_W \gamma_{ij} - C_N \eta_{ij} \quad , \quad (11)$$

where the base tensors are defined as $\beta_{ij} \stackrel{\text{def}}{=} 2\bar{\Delta}^2 |\bar{S}| \bar{S}_{ij}$, $\gamma_{ij} \stackrel{\text{def}}{=} 4\bar{\Delta}^2 (\bar{S}_{ik} \bar{\Omega}_{kj} + \bar{S}_{jk} \bar{\Omega}_{ki})$ and $\eta_{ij} \stackrel{\text{def}}{=} 4\bar{\Delta}^2 (\bar{S}_{ik} \bar{S}_{kj} - \bar{S}_{mn} \bar{S}_{nm} \delta_{ij} / 3)$. Here, $\bar{\Omega}_{ij} \stackrel{\text{def}}{=} (\partial \bar{u}_i / \partial x_j - \partial \bar{u}_j / \partial x_i) / 2$ is the resolved rotation rate tensor. The model coefficients are dynamically calibrated using local instantaneous flow variables following the least-square approach as

$$\begin{bmatrix} M_{ij} M_{ij} & M_{ij} W_{ij} & M_{ij} N_{ij} \\ W_{ij} M_{ij} & W_{ij} W_{ij} & W_{ij} N_{ij} \\ N_{ij} M_{ij} & N_{ij} W_{ij} & N_{ij} N_{ij} \end{bmatrix} \cdot \begin{bmatrix} C_S \\ C_W \\ C_N \end{bmatrix} = - \begin{bmatrix} \mathcal{L}_{ij}^* M_{ij} \\ \mathcal{L}_{ij}^* W_{ij} \\ \mathcal{L}_{ij}^* N_{ij} \end{bmatrix} \quad (12)$$

where $W_{ij} \stackrel{\text{def}}{=} \lambda_{ij} - \gamma_{ij}$ and $N_{ij} \stackrel{\text{def}}{=} \zeta_{ij} - \eta_{ij}$ are differential tensors, respectively (analogous to the definition of M_{ij}); and $\lambda_{ij} \stackrel{\text{def}}{=} 4\bar{\Delta}^2 (\bar{S}_{ik} \bar{\Omega}_{kj} + \bar{S}_{jk} \bar{\Omega}_{ki})$ and $\zeta_{ij} \stackrel{\text{def}}{=} 4\bar{\Delta}^2 (\bar{S}_{ik} \bar{S}_{kj} - \bar{S}_{mn} \bar{S}_{nm} \delta_{ij} / 3)$ are base tensors at the test-grid level.

2.2. Boundary Conditions

No slip boundary condition is used for all solid surfaces and periodic boundary condition has been applied to the domain boundaries in spanwise direction. Neumann boundary condition is applied to the outlet boundary. One of the major challenges for this problem is to prescribe a realistic inlet boundary condition that would allow the LES to reproduce the wind-tunnel experiment of Brown et al. [4] in a precise manner. The mean velocity profile at the inlet is considered to follow the power-law profile given by

$$u = u_\infty \left(\frac{y}{0.15} \right)^{0.16} \quad \text{with} \quad u_\infty = 3 \text{ m/s}. \quad (13)$$

Since the purpose of the original experiment was to simulate a deep rough-wall atmospheric boundary layer, the approaching flow has exceptionally high turbulence level. In fact, the lowest turbulence intensity at the domain inlet and above the cubes is approximately 10%. In order to reproduce the high turbulence level using LES, four methods have been tested for modeling the inlet boundary, which include: A) prescribing mean profile with no fluctuations, B) using a turbulent plane channel flow simulation as a precursor, C) using a solid grid at the inlet plane of the domain, and D) using a solid grid at the inlet plane with superimposed correlated random fluctuations in regions above the cubes.

In order to evaluate the performances of these four inlet boundary condition methods, the profiles of the streamwise root-mean-squared (RMS) velocity predicted by LES at a typical point ($x/h = 9.5$) are compared against the experimental data. As evident in figure 3, method A cannot generate any turbulence above the cubes. As an improvement, method B can generate turbulence above the cubes but it is still far from the high turbulence level measured in the experiment. The approach for method C is drastically different than that for method B, however, its

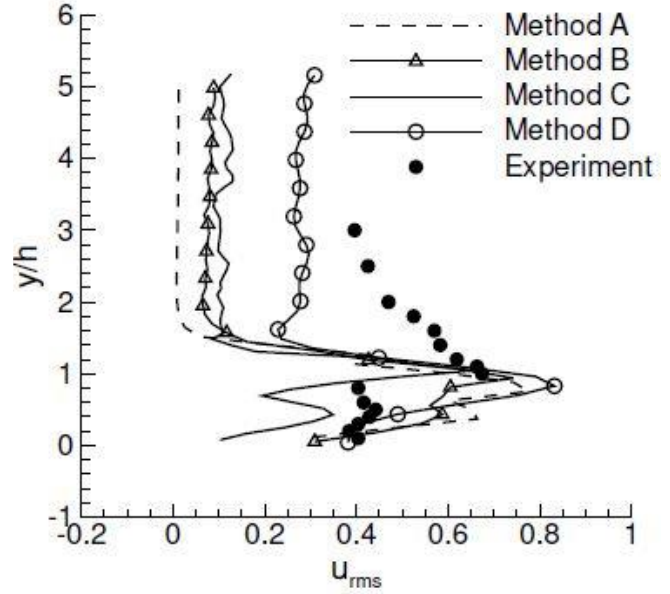


Fig. 3: Effects of 4 different inlet conditions on the streamwise RMS velocity level at the location $x/h = 9.5$.

performance is not considerably different from method B. Based on the observation that methods A, B and C all fail to reproduce the high turbulence level above the cubes, we propose method D, which superimposes correlated random numbers in regions above the wall-mounted cubes ($x/h > 3$ and $y/h > 1.35$) based on the approach of method C. The superposition is implemented at the beginning of consecutive time-windows. The duration of each time-window is 0.03 seconds which is 60% of the time required for the mean flow to travel one cube side. With such arrangement, method D is able to reproduce the highest turbulence level above the cube (closest to the measured value). The results reported in this paper is based on method D.

3. Results and discussion

In this section we will present the qualitative and quantitative results to conduct physical analysis and investigate the flow structure over the array of cubes. Velocity and pressure contours, vector plots, Energy spectra and comparison of turbulence statistics will be used to conduct the analysis.

3.1. Qualitative results

In order to provide a qualitative physical insight about the general flow structure, a typical snapshot of the flow field is taken to present instantaneous contours and vector plots from the lateral and top views. The results are obtained from a simulation which uses the DNM as its SGS stress model. Fig. 4 shows the instantaneous streamwise velocity contour in the x - y plane located at $z/h = 0$. As evident in the figure, a stagnant region has been formed in the impinging zone of the first row. The strong shear layer arising from velocity difference in regions above the cubes are observable in the figure. Because of the matrix configuration of the cubes, no reattachment occurs behind

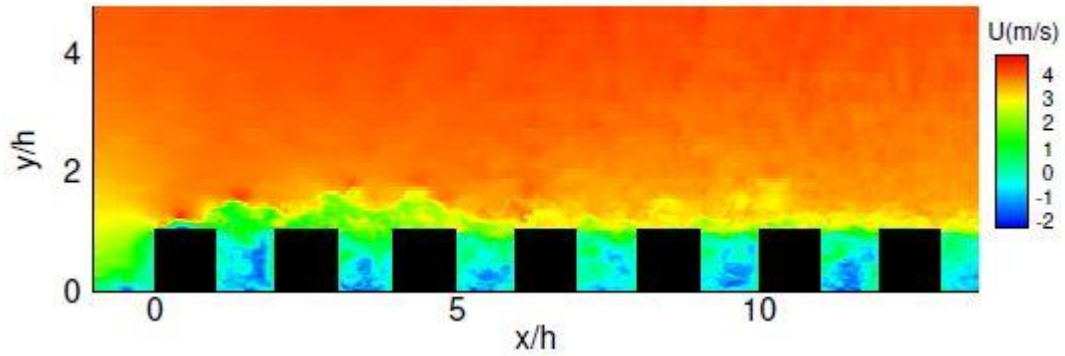


Fig. 4: Lateral view of a typical instantaneous streamwise velocity contours.

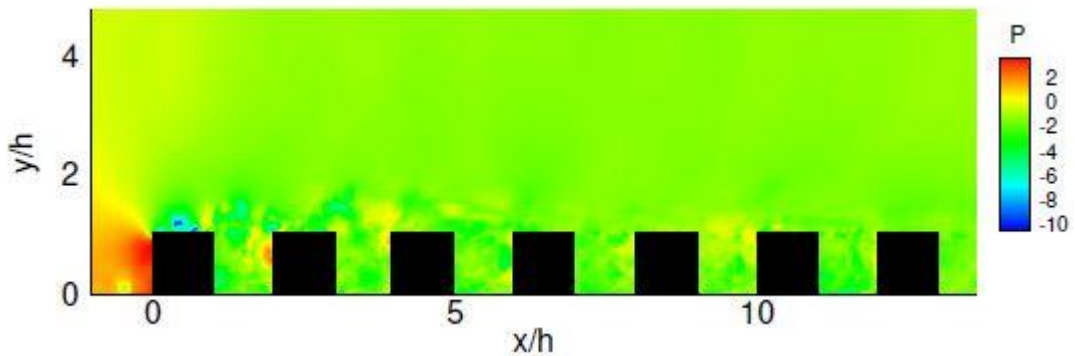


Fig. 5: Lateral view of a typical instantaneous pressure contours.

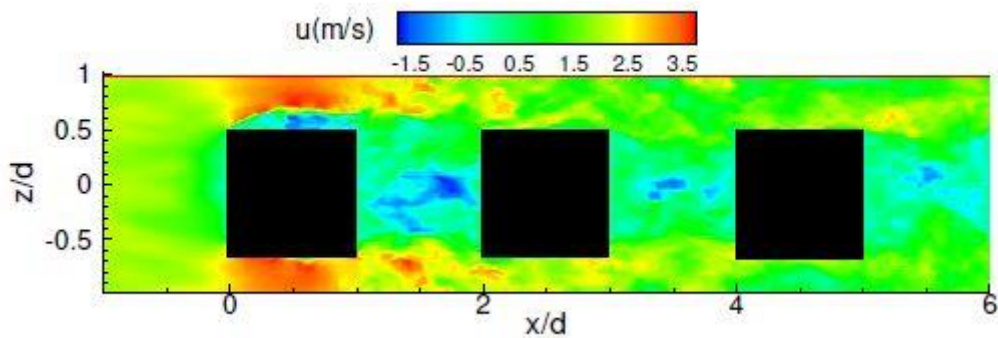


Fig.6: Top view of a typical instantaneous velocity contours.

any of the first 6 rows and the flow is recirculating inside the space between two cubes. This shows that one h spacing is not enough for flow recovery after the cubes. Fig. 5 presents the static pressure contours extracted from the same instantaneous field in the same x-y plane. A high pressure region corresponding to the impinging flow is observable in front of the first row. Tip vortex shedding from the rooftop of the first row is also observable. However, since the next rows have been placed in the wake of the first row, no tip vortex shedding is present at their rooftops. In view of this, the high momentum approaching flow strikes the windward of the first row and this will lead to the tip vortex shedding occurring at the first row rooftop. After the flow impingement with the first row, a strong shear layer will be produced on its top edge which stops the tip vortex shedding from the rooftop of the next rows.

Figs 6 and 7 present the streamwise velocity and pressure contours in the x-z plane located at $y/h = 0.5$ extracted from the same instantaneous field. Local flow acceleration occurring in side regions of the first row is clearly observable in figure 6. Lateral vortex shedding is also occurring only for the first row which is shown in figure 7. The high pressure region in the impingement region is also observable in figure 7. Fig. 8 depicts the velocity vector plot in the wake region of all the rows in the same x-z plane. Two small lateral vortices adjacent to the side walls are only observable for the first row which are corresponding to the lateral vortex shedding of the first row. Two large counter-rotating vortices are observable in the wake region of the first six rows with a fairly similar qualitative pattern. For the last row, the counter-rotating vortices have been more elongated in the streamwise direction which

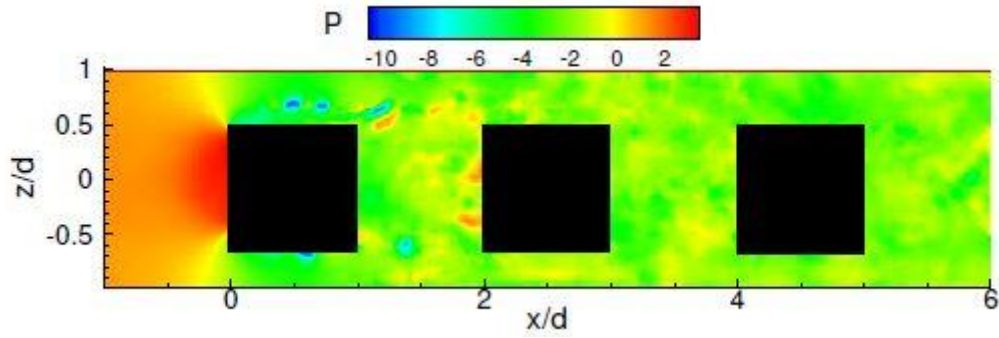
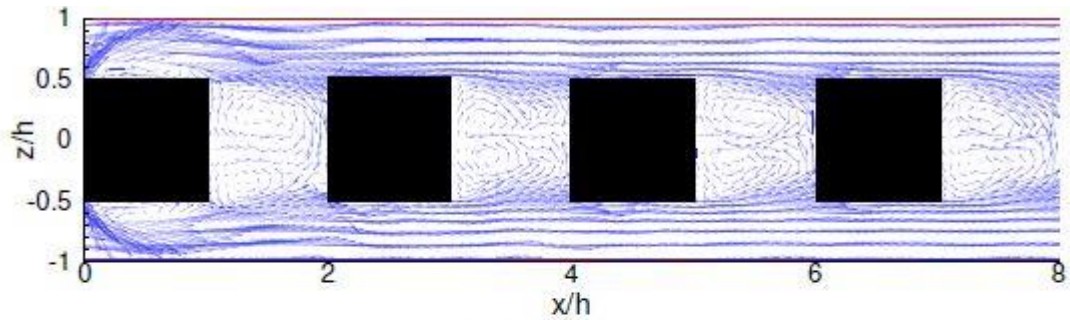
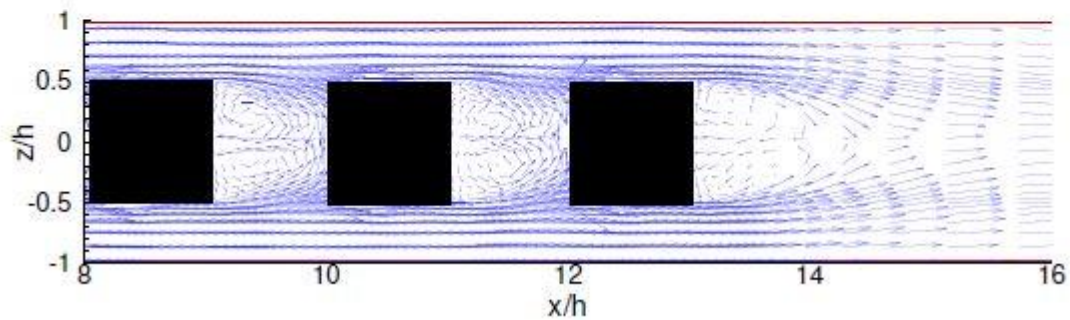


Fig. 7: Top view of a typical instantaneous pressure contours.

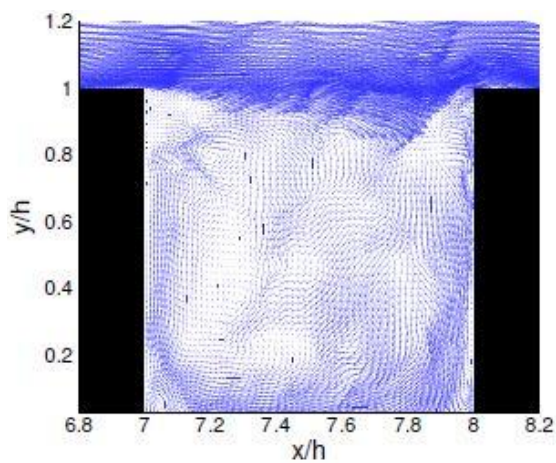


(a) $0 < x/h < 8$

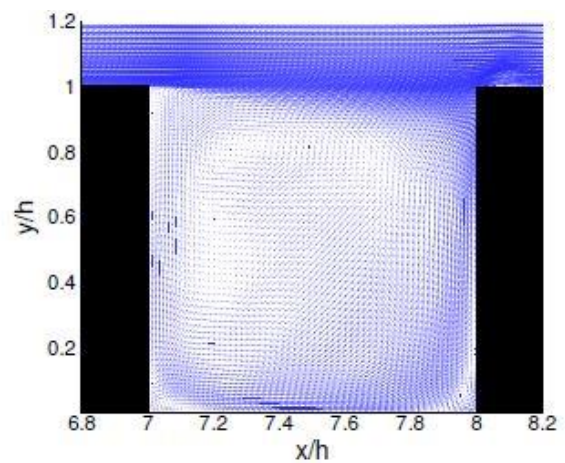


(b) $8 < x/h < 16$

Fig. 8: Vector plot of the velocity field in the wake region of the cubes from the top view.



(a) instantaneous



(b) Mean

Fig. 9: Vector plot of the velocity field in the canyon region between rows 4 and 5

is due to the open space after the last row of cubes. After the last row, the distance required for the streamlines

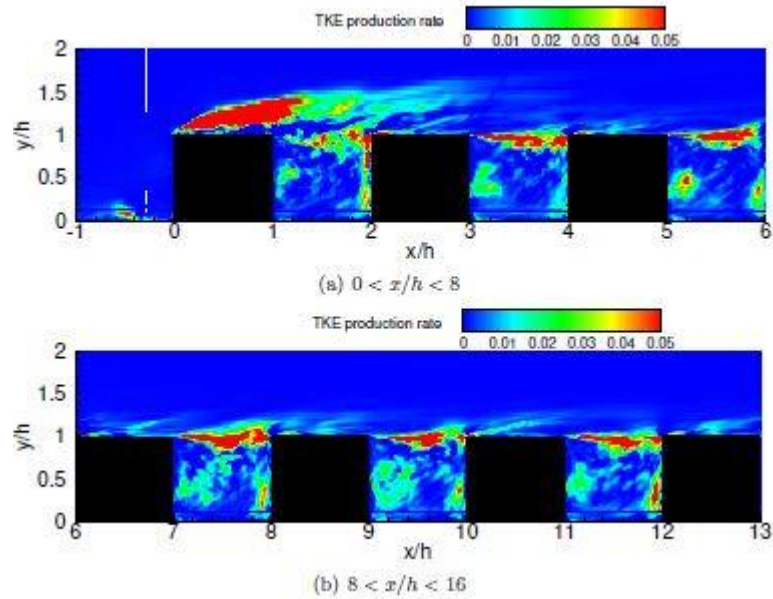


Fig. 10: Lateral view of TKE production contours (non-dimensionalized with the maximum TKE production in the same plane).

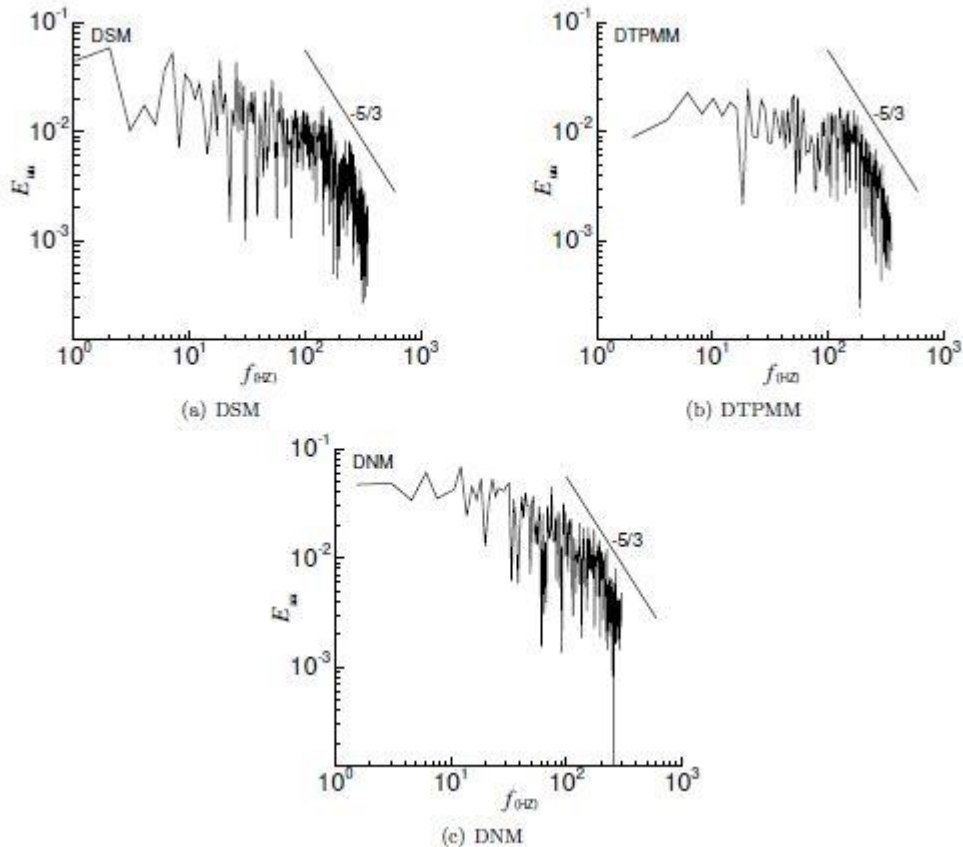


Fig. 11: Temporal energy spectra for streamwise velocity obtained from simulations with three SGS models at $x/h = 5.5$ and $y/h = 1.0$.

to take their streamwise direction is approximately $3h$. This, again, indicates that the one h spacing between two consecutive cubes is not enough for the full flow recovery. Fig. 9a magnifies the instantaneous velocity vector map between rows 4 and 5. As evident in this figure, several small local vortices are formed in that region which clearly shows

the turbulent flow structures and irregular flow patterns. In figure 9b, the time-averaged vector map at the same location is shown in which only one large vortex in the core region and two small vortices at the corners are observable.

Fig. 10 shows the contours of TKS production rate from the lateral view. As evident in figure 10a, the maximum value

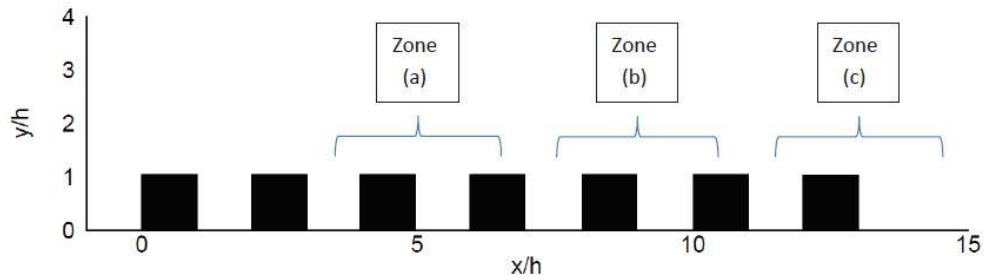


Fig. 12: Locations of three different zones in the x-direction.

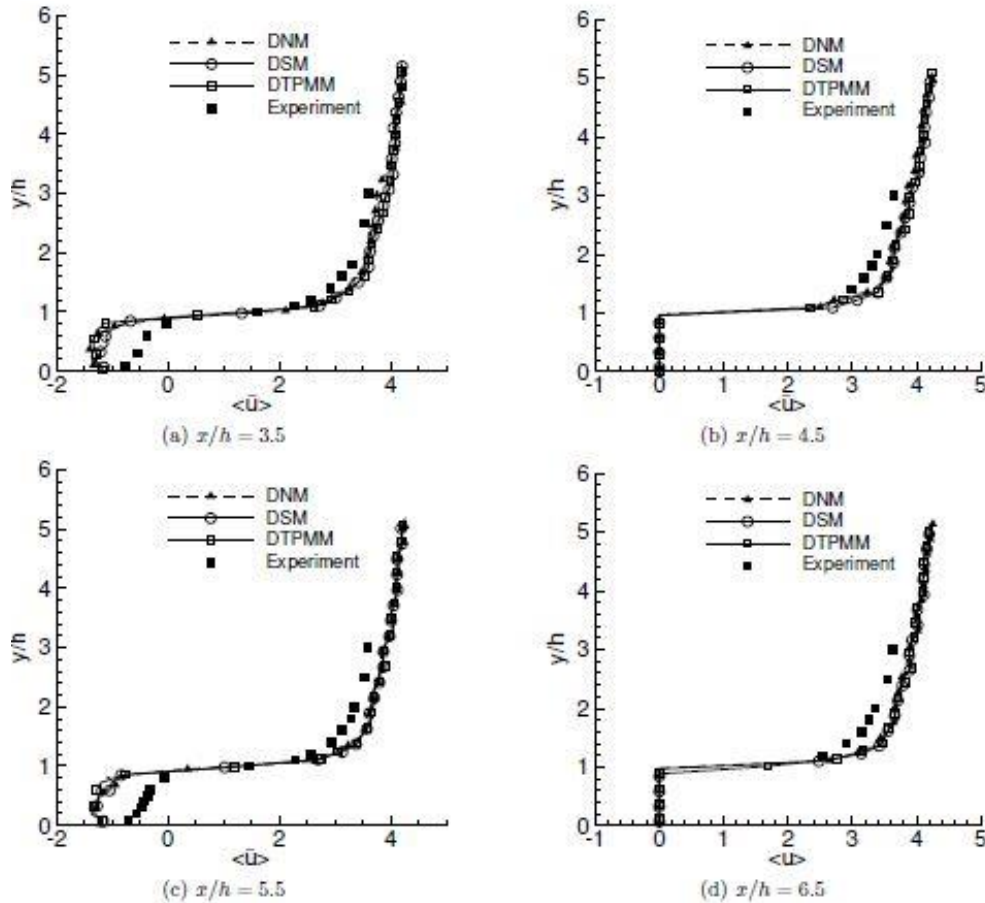


Fig. 13: Profiles of the mean streamwise velocity at different x-locations in the zone (a).

for TKE production occurs at the rooftop edge of the first building row. This is mainly because of the flow separation at this location as a consequence of the high velocity gradient. The high velocity gradient is the result of the impact of the flow to the sharp edge of the first row. This flow separation can also be observed in figure 5 in which the tip vortex shedding from the rooftop of the first row is observable. After the second row, a band of high TKE production can be observed right above all canyon regions at the elevation $y/h \approx 1$. This high value of TKE production is mainly due to the boundary-layer separation formed on the rooftop of the obstacles.

Fig. 11 shows the temporal streamwise energy spectra at $x/h = 5.5$ and $y/h = 1.0$ obtained from simulations

with three SGS models. From the figure, it is evident that simulations based on all three SGS stress models have been able to capture the inertial subrange. Furthermore, a perusal of three subfigures indicates that the resolved streamwise TKE predicted by the DNM is the largest at all frequencies. This suggests that the DNM has the lowest energy dissipation among the SGS models considered in this research.

3.2. Turbulence statistics

In this section, first- and second-order turbulence statistics inside and above the canyon regions will be investigated. Three separate zones will be considered to analyze the state of the flow in different regions. Fig. 12 schematically presents the

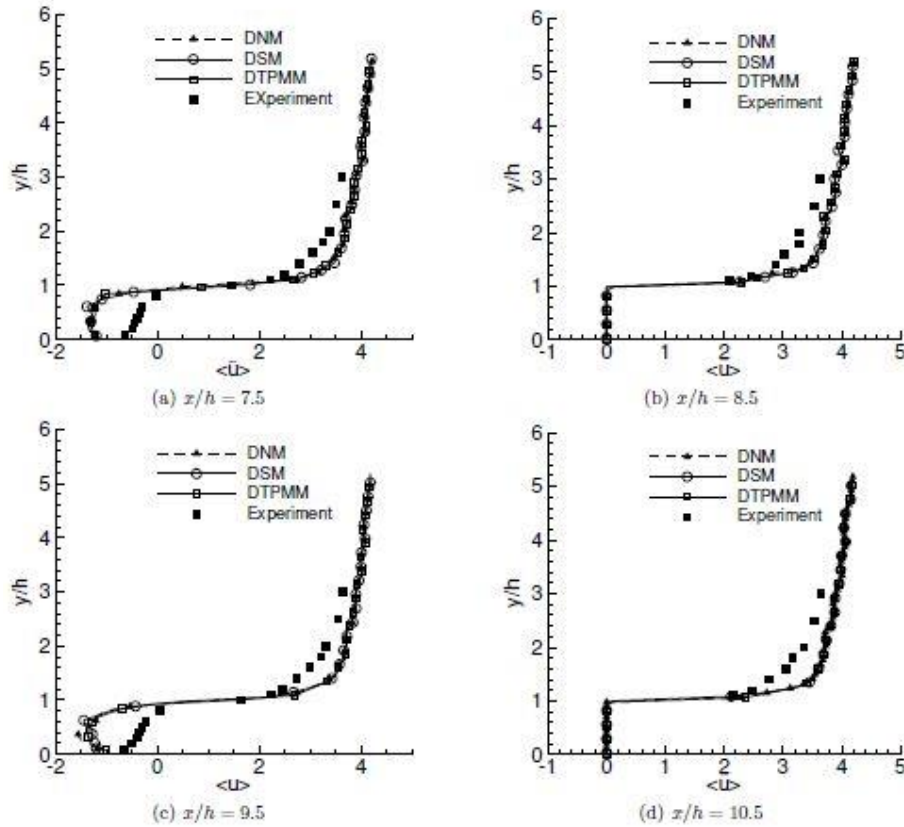


Fig. 14: Profiles of the mean streamwise velocity at different x-locations in the zone (b).

zones. The streamwise range for each zone is as follows: $3.5 < x/h < 6.5$, $7.5 < x/h < 10.5$ and $11.5 < x/h < 14.5$ for zones (a), (b) and (c), respectively. Zone (a) starts after the second row of the array and is considered as the developing zone. Fig. 13 shows the mean streamwise velocity profile inside the canyon (at $x/h = 4.5$ and 6.5) and above the rooftop (at $x/h = 4.5$ and 6.5) of the array in zone (a). A good agreement between the simulation and the experimental results can be observed for both canyon and rooftop regions. In terms of the prediction of $\overline{h\bar{u}}$, no significant effect is observed arising from using different SGS models. As shown in figures 13a and 13c, in the street canyon, LES overpredicts the magnitude of the negative velocity (corresponding to the recirculation flow). The discrepancy is due to two main reasons: first, velocity measurement in regions very close to solid surfaces is a very difficult job to do especially with hot-wire systems. This may lead to a reduced accuracy of the experimental measurements inside the canyon region. Second, numerical dissipation and false diffusion may become significant in wake flows when the flow is highly mixing and three dimensional which indicates the need for highly accurate and higher order numerical schemes when fine flow structures are intended to be captured. The mentioned discrepancy also exists for the velocity profiles in zone (b) shown in Fig. 14. In figure 16, the RMS profiles of the streamwise velocity are shown for the same locations. For both canyon and rooftop regions, the maximum turbulence level occurs around the cube rooftop ($y/h \approx 1$).

This peak value in the resolved TKE is the result of the strong shear production at the rooftop of the cube. This fact is consistent with the distribution of TKE production rate presented in figure 10. The u_{rms} around the cube rooftop is fairly well captured by all numerical simulations, however, the turbulence level above the cube is under-predicted by numerical simulations and it decays quickly as the vertical distance from the rooftop increases. Fig. 19 presents the profiles of the vertical RMS velocity at different locations in zone (a). A good agreement between the numerical prediction and experimental measurement of v_{rms} can be observed for both canyon regions (corresponding to figures 19a and 19c) and rooftop regions (corresponding to figures 19b and 19d). According to the findings of Hanna et al. [21], a self-similar behavior should be observable after the third or fourth row. However, in the current case study, the self-similar behavior for the mean streamwise velocity has been observed after the second row (zone (a)) for both experimental and numerical results. Zone (b), which starts after the forth row at $x/h = 7.5$ and extends up to the sixth row at $x/h = 10.5$, again shows self-similar profiles of the mean streamwise velocity as exhibited in figure 14. Figs 17 and 20 show the profiles of the streamwise and vertical RMS velocity at different locations in zone (b). No significant difference between the profiles of RMS velocities can be observed between zone (a) and zone (b). This fact reconfirms the self-similar flow structures starting at zone (a). Zone (c) which includes the last row and its wake

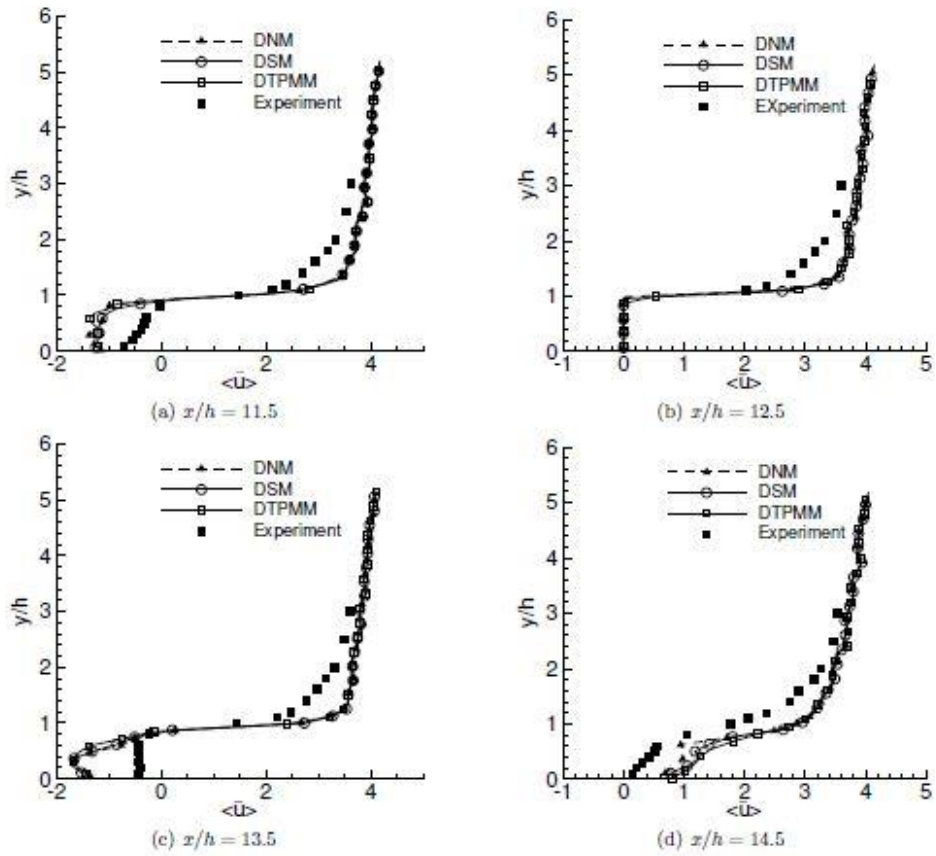


Fig. 15: Profiles of the mean streamwise velocity at different x-locations in the zone (c).

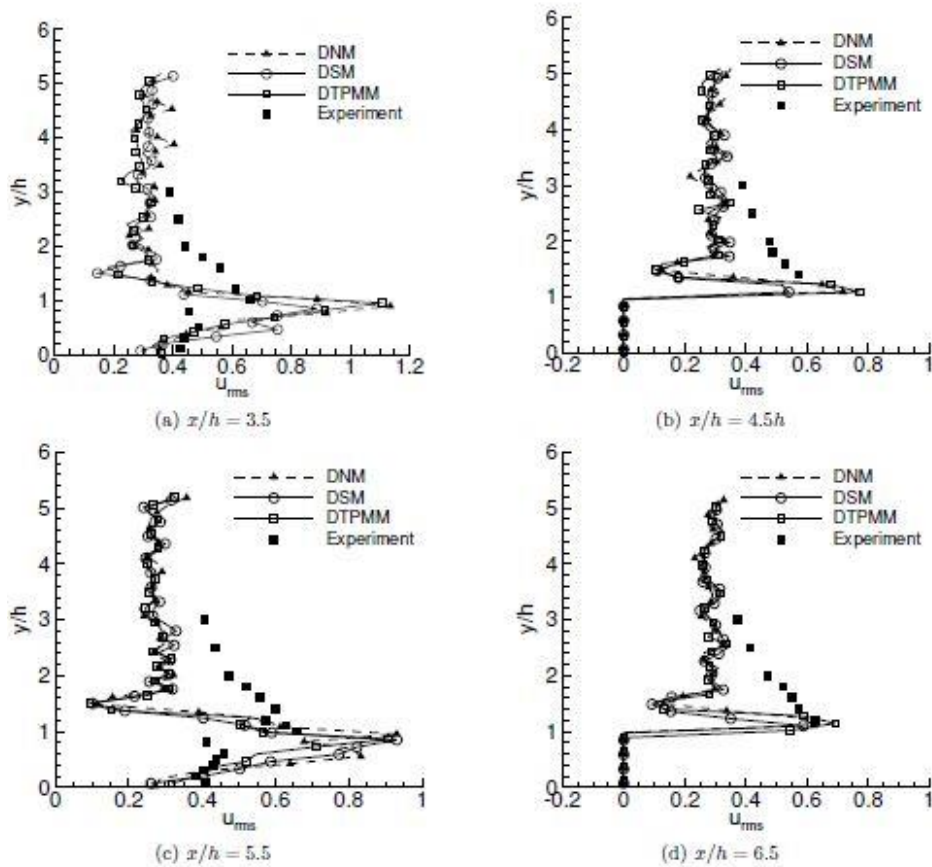


Fig. 16: Profiles of the streamwise RMS velocity at different x-locations in the zone (a).

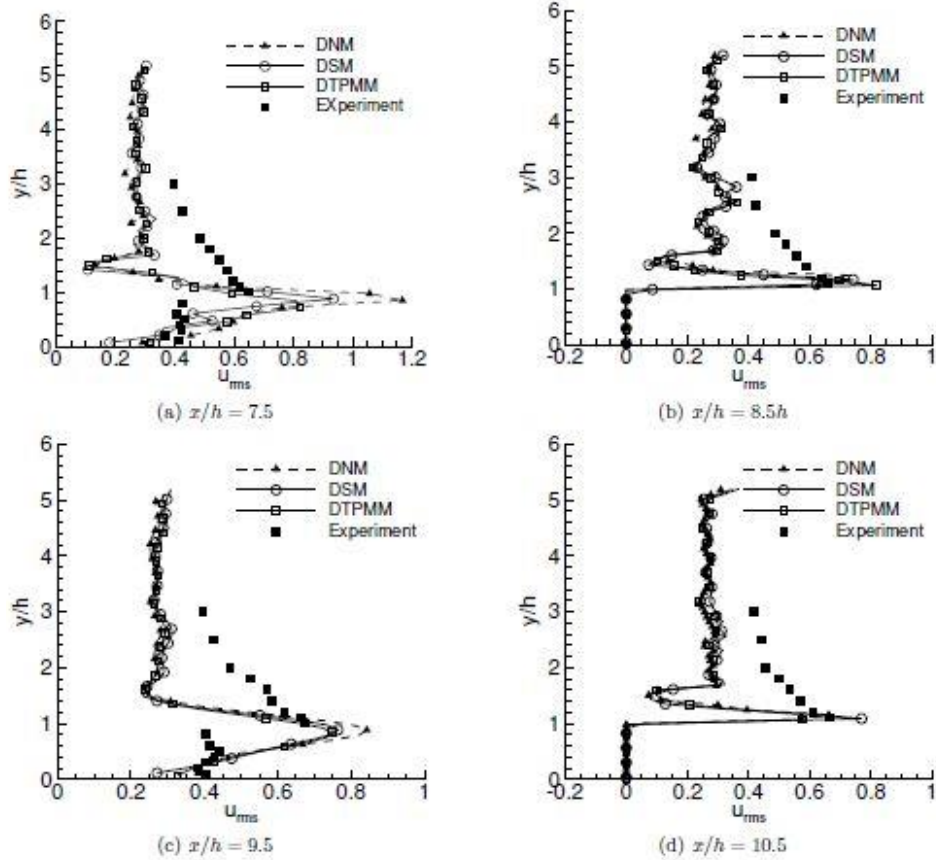


Fig. 17: Profiles of the streamwise RMS velocity at different x-locations in the zone (b).

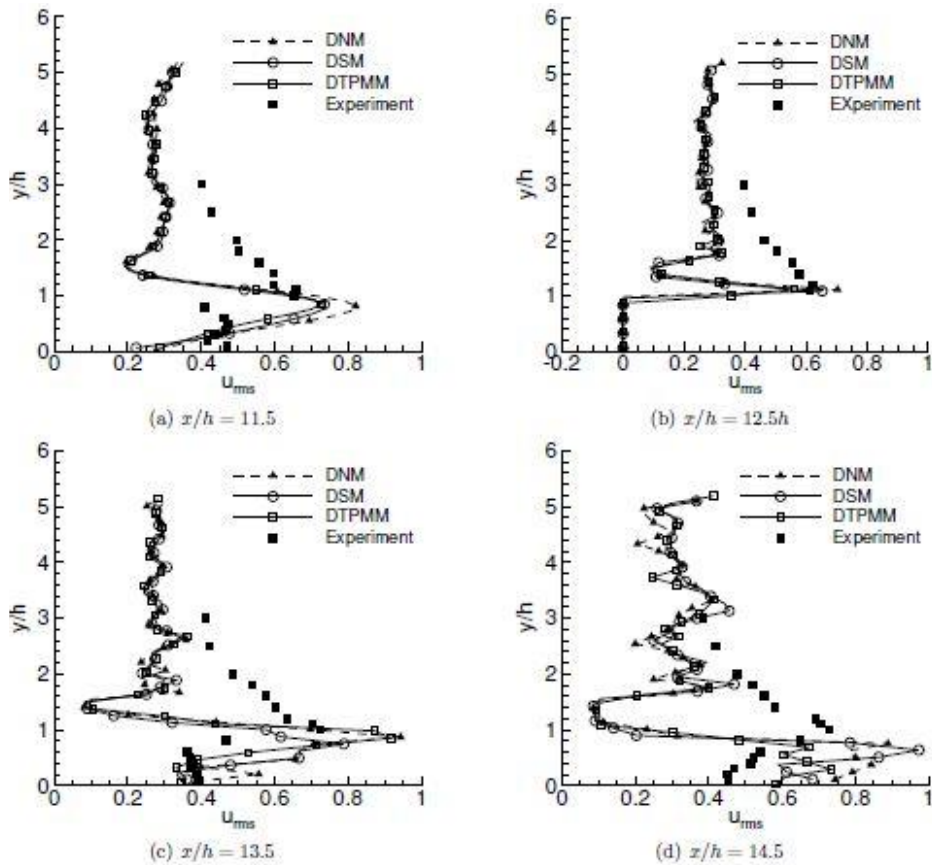


Fig. 18: Profiles of the streamwise RMS velocity at different x-locations in the zone (c).

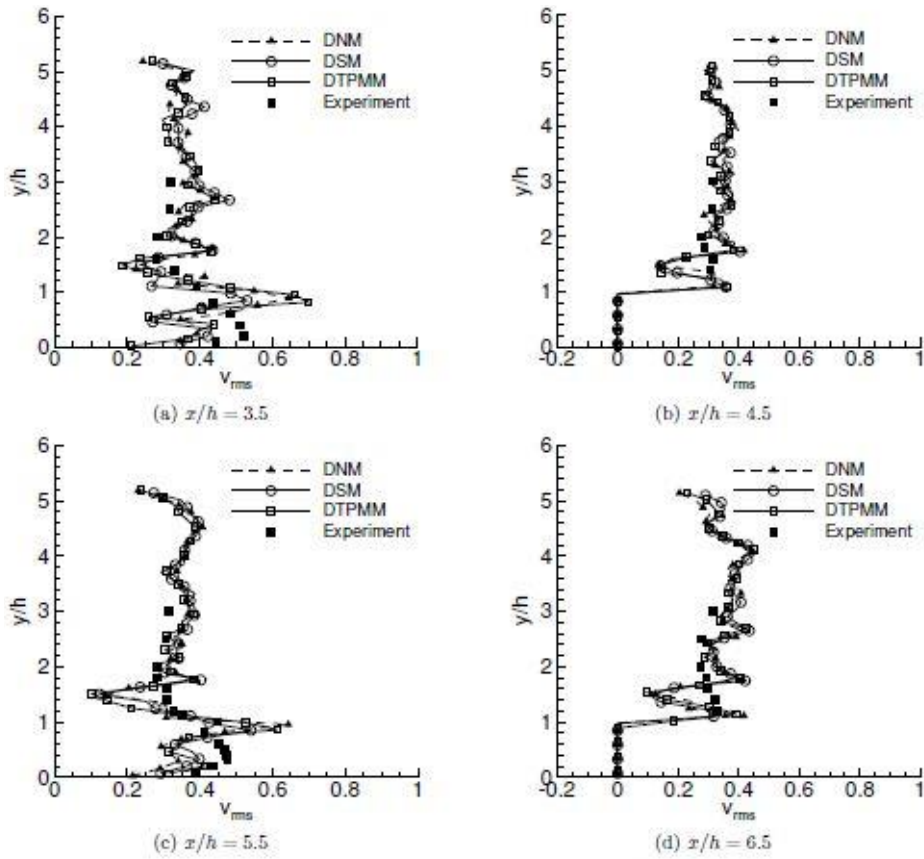


Fig. 19: Profiles of the vertical RMS velocity at different x-locations in the zone (a).

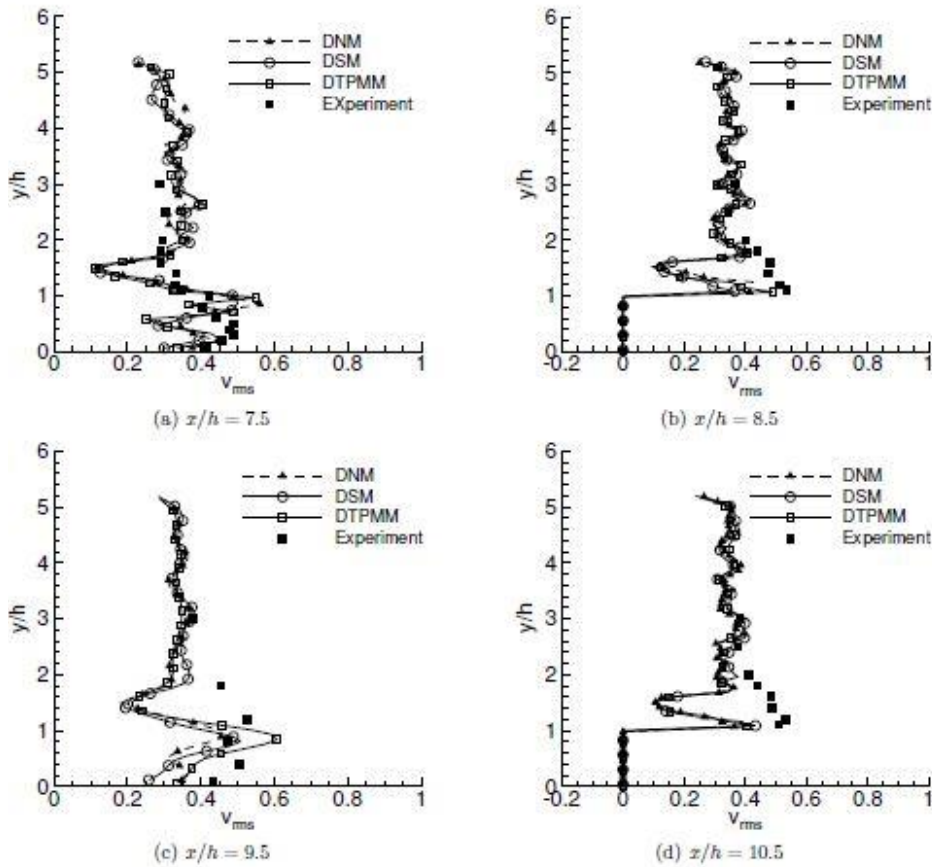


Fig. 20: Profiles of the vertical RMS velocity at different x-locations in the zone (b).

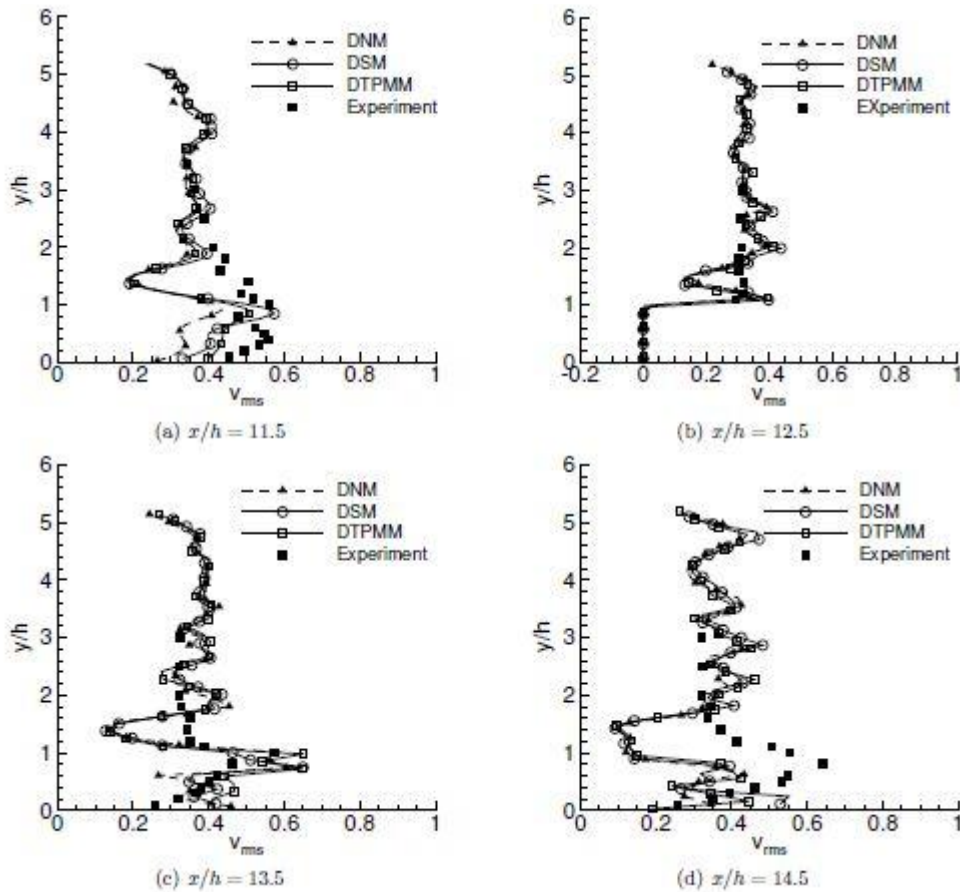


Fig. 21: Profiles of the vertical RMS velocity at different x-locations in the zone (c).

region starts at $x/h = 11.5$ and extends up to $x/h = 14.5$. Fig. 15 shows the profiles of the mean streamwise velocity at different locations of zone (c). At $x/h = 13.5$ which is $0.5h$ away from the leeward of the last row, Numerical prediction exhibits over-prediction of negative velocity in the recirculation region. At $x/h = 14.5$, no negative velocity is observed showing that flow reattachment has been occurred.

4. Conclusions

Large-eddy simulation of turbulent flow over an array of wall-mounted cubic obstacles at $Re = 30,000$ is conducted using three SGS models. In order to reproduce the exceptionally high turbulence level (with a minimum turbulence intensity of 10%) of the neutrally stratified atmospheric boundary layer simulated in the wind tunnel, four methods have been tested to model the inlet boundary condition. It is observed that use of different inlet conditions can significantly affect the streamwise turbulence intensity (u_{rms}) profile. The proposed method based on mounting a solid grid at the inlet and superimposing correlated random fluctuations in regions above the cubes is shown to be very effective in generating sustained high turbulence levels. Time-averaged first- and second-order flow statistics do not show much sensitivity towards the SGS models tested. With respect to the temporal energy spectra of the streamwise velocity at a typical canyon location, the results from simulations with different SGS models are also similar, however, the DTPMM

shows the lowest predicted energy level and the DNM shows the highest predicted level. It is also shown based on the time-averaged flow patterns and also turbulence statistics that the self-similar region in the array of cubes starts after the second row of wall-mounted cubes.

References

- [1] I. P. Castro and A. G. Robins. The flow around a surface-mounted cube in uniform and turbulent streams. *J. Fluid Mech.*, 79:307–335, 1977.
- [2] A. Okajima. Strouhal numbers of rectangular cylinders. *J. Fluid Mech.*, 123:379–398, 1982.
- [3] H. J. Hussein and R. J. Martinuzzi. Energy balance for turbulent flow around a surface mounted cube placed in a channel. *Phys. Fluids*, 8:764–780, 1996.
- [4] M. J. Brown, R. E. Lawson, D. S. DeCroix, and R. L. Lee. Comparison of centerline velocity measurements obtained around 2D and 3D building arrays in a wind tunnel. Technical Report LA-UR-01-4138, Los Alamos National Laboratory, 2001.
- [5] D. Sumner, J. L. Heseltine, and O. J. P. Dansereau. Wake structure of a finite circular cylinder of small aspect ratio. *Exper. Fluids*, 37:720–730, 2004.
- [6] M. S. Adaramola, O. G. Akinlade, D. Sumner, D. J. Bergstrom, and A. J. Schenstead. Turbulent wake of a finite circular cylinder of small aspect ratio. *J. Fluids Struct.*, 22:919–928, 2006.
- [7] D. Sumner and J. L. Heseltine. Tip vortex structure for a circular cylinder with a free end. *J. Wind Eng. Ind. Aero.*, 96:1185–1196, 2008.
- [8] R. J. Martinuzzi and B. Havel. Vortex shedding from two surface-mounted cubes in tandem. *Int. J. Heat Fluid Flow*, 25:364–372, 2004.
- [9] D. Sumner, M. D. Richards, and O. O. Akosile. Strouhal number data for

- two staggered circular cylinders. *J. Wind Eng. Ind. Aero.*, 96:859–871, 2008.
- [10] H. C. Lim, I. P. Castro, and R. P. Hoxey. Bluff bodies in deep turbulent boundary layers: Reynolds-number issues. *J. Fluid Mech.*, 571:97–118, 2007.
- [11] H. Wang, Y. Zhou, C. Chan, and T. Zhou. Momentum and heat transport in a finite-length cylinder wake. *Exper. Fluids*, 46:1173–1185, 2009.
- [12] H. F. Wang and Y. Zhou. The finite-length square cylinder near wake. *J. Fluid Mech.*, 638:453–490, 2009.
- [13] P. Sattari, J. A. Bourgeois, and R. J. Martinuzzi. On the vortex dynamics in the wake of a finite surface-mounted square cylinder. *Exper. Fluids*, 52:1149–1167, 2012.
- [14] J. A. Bourgeois, P. Sattari, and R. J. Martinuzzi. Alternating half-loop shedding in the turbulent wake of a finite surface-mounted square cylinder with a thin boundary layer. *Phys. Fluids*, 23:095101, 1–15, 2011.
- [15] F. S. Lien, E. Yee, and Y. Cheng. Simulation of mean flow and turbulence over a 2D building array using high-resolution CFD and a distributed drag force approach. *J. Wind Eng. Ind. Aero.*, 92:117–158, 2004.
- [16] F.-S. Lien and E. Yee. Numerical modelling of the turbulent flow developing within and over a 3-D building array, part I: A high resolution Reynolds-averaged Navier-Stokes approach. *Boundary-Layer Meteorol.*, 112:427–466, 2004.
- [17] J. L. Santiago, A. Martilli, and F. Martín. CFD simulation of airflow over a regular array of cubes. Part I: Three-dimensional simulation of the flow and validation with wind-tunnel measurements. *Boundary-Layer Meteorol.*, 122:609–634, 2007.
- [18] K. B. Shah and J. H. Ferziger. A fluid mechanics view of wind engineering: Large eddy simulation of flow past a cubic obstacle. *J. Wind Eng. Ind. Aero.*, 67:211–224, 1997.
- [19] R. Martinuzzi and C. Tropea. The flow around surface-mounted, prismatic obstacles placed in a fully developed channel flow. *J. Fluids Eng.*, 115:85–92, 1993.
- [20] S. Schmidt and F. Thiele. Comparison of numerical methods applied to the flow over wall-mounted cubes. *Int. J. Heat Fluid Flow*, 23:330–339, 2002.
- [21] S. R. Hanna, S. Tehranian, B. Carissimo, R. W. MacDonald, and R. Lohner. Comparisons of model simulations with observations of mean flow and turbulence within simple obstacle arrays. *J. Atmos. Env.*, 36:5067–5079, 2002.
- [22] B. Ničeno, A. D. T. Dronkers, and K. Hanjalić. Turbulent heat transfer from a multi-layered wall-mounted cube matrix: A large eddy simulation. *Int. J. Heat Fluid Flow*, 23:173–185, 2002.
- [23] Y. Cheng, F. S. Lien, E. Yee, and R. Sinclair. A comparison of large eddy simulations with a standard $k-\epsilon$ Reynolds-averaged Navier-Stokes model for the prediction of a fully developed turbulent flow over a matrix of cubes. *J. Wind Eng. Ind. Aero.*, 91:1301–1328, 2003.
- [24] I. Afgan, C. Moulinec, R. Prosser, and D. Laurence. Large eddy simulation of turbulent flow for wall mounted cantilever cylinders of aspect ratio 6 and 10. *Int. J. Heat Fluid Flow*, 28:561–574, 2007.
- [25] R. F. Shi, G. X. Cui, Z. S. Wang, C. X. Xu, and Z. S. Zhang. Large eddy simulation of wind field and plume dispersion in building array. *J. Atmos. Env.*, 42:1083–1097, 2008.
- [26] J. H. Lee, H. J. Sung, and P. A. Krogstad. Direct numerical simulation of the turbulent boundary layer over a cube-roughened wall. *J. Fluid Mech.*, 669:397–431, 2011.
- [27] M. Saeedi and B.-C. Wang. Large-eddy simulation of turbulent flow over an array of wall-mounted cubic obstacles. In *Direct and Large-Eddy Simulation 9 (DLES9)*, 2013. Dresden, Germany.
- [28] R. K. Madabhushi and S. P. Vanka. Large eddy simulation of turbulence-driven secondary flow in a square duct. *Phys. Fluids A*, 3:2734–2745, 1991.
- [29] P. Sagaut. *Large Eddy Simulation for Incompressible Flows: An Introduction*. Springer, Berlin, 2nd edition, 2002.
- [30] F. E. Ham, F. S. Lien, and A. B. Strong. A fully conservative second-order finite difference scheme for incompressible flow on nonuniform grids. *J. Comp. Phys.*, 177:117–133, 2002.
- [31] M. Germano, U. Piomelli, P. Moin, and W. H. Cabot. A dynamic subgrid-scale eddy viscosity model. *Phys. Fluids A*, 3:1760–1765, 1991.
- [32] D. K. Lilly. A proposed modification of the Germano subgrid-scale closure method. *Phys. Fluids A*, 4:633–635, 1992.
- [33] Y. Morinishi and O. V. Vasilyev. A recommended modification to the dynamic two-parameter mixed subgrid scale model for large eddy simulation of wall bounded turbulent flow. *Phys. Fluids*, 13:3400–3410, 2001.
- [34] B.-C. Wang and D. Bergstrom. A dynamic nonlinear subgrid-scale stress model. *Phys. Fluids*, 17:035109, 1–15, 2005.

HOW TO CITE THIS ARTICLE

M. Saeedi, *Large-eddy simulation of turbulent flow over an array of wall-mounted cubes submerged in an emulated atmospheric boundary-layer*, *AUT J. Model. Simul.*, 51(2) (2019) 163-178.

DOI: [10.22060/miscj.2019.15614.5137](https://doi.org/10.22060/miscj.2019.15614.5137)



